MODEL-BASED COMPARISON OF 3D VOLUMETRIC CURVATURE AND COHERENCE WITH A CO-RENDERING APPLICATION

XUEHUA CHEN[1,2], WEI YANG[2], ZHENHUA HE[2] and WENLI ZHONG[3]

[1] *State Key Laboratory of Oil & Gas Reservoir Geology and Exploitation, Chengdu University of Technology, #1 Erxianqiao Dongsan Road, Chengdu, Sichuan 610059, P.R. China. chen_xuehua@163.com*
[2] *College of Geophysics, Chengdu University of Technology, #1 Erxianqiao Dongsan Road, Chengdu, Sichuan 610059, P.R. China.*
[3] *College of Earth Sciences, Chengdu University of Technology, #1 Erxianqiao Dongsan Road, Chengdu, Sichuan 610059, P.R. China. zhongwenli07@cdut.cn*

(Received July 30, 2011; revised version accepted December 26, 2011)

ABSTRACT

Chen, X., Yang, W., He, Z. and Zhong, W., 2012. Model-based comparison of 3D volumetric curvature and coherence with a co-rendering application. *Journal of Seismic Exploration*, 21: 000-102.

Coherence and curvatures are both important attributes for the delineation of geological features of interest in seismic data. To clarify the response of these attributes to different geological features and to better integrate them into seismic interpretation, we first presented an algorithm of 3D volumetric curvature. Next, by using two modified "French" models to simulate a variety of typical geological features, we compare the spatial relationships between geological anomalies of interest and the response of these two types of attributes; in doing so, we visually analyze the differences and similarities between these attributes. Then, by discriminately manipulating the transparency of different values in these two attributes, a combined visualization of co-rendered 3D volumetric curvature with coherence is introduced. The work presented in this paper provides a better understanding of these attributes and the spatial relationships between these attributes and geological features in real seismic data. Field data examples demonstrate that the co-rendering method can effectively communicate information, fully extract and highlight geological anomalies, and attenuate the noisy background in these attributes.

KEY WORDS: 3D volumetric curvature, coherence, attributes co-rendering, geologic model, fault detection.

0963-0651/12/$5.00

INTRODUCTION

Curvature and coherence are two important seismic geometric attributes. The coherence attribute delineates seismic singularities by measuring lateral differences in discontinuity, or semblance, in seismic waveforms. Examples include the cross-correlation-based C1 algorithm (Bahorich and Farmer,1995), the semblance-based C2 algorithm (Marfurt et al., 1998), and the eigenstructure-based C3 algorithm (Gersztenkorn and Marfurt, 1999). These three algorithms can be unified with a covariance matrix (Marfurt et al., 1999).

The curvature attribute is a recently introduced method for geological structure interpretation and reservoir analysis by measuring stratal bending (Roberts, 2001; Chopra and Marfurt, 2007). It is sensitive to bending related to tectonic deformation. Curvature is a powerful tool for mapping complex fault, fracture, channel and structural bending. It has attracted widespread attention in recent years (Chopra and Marfurt, 2007a; 2007b; 2008; Flierman et al., 2008; Buck et al., 2007). The correlation of Gaussian curvature to open fractures measured on an outcrop was studied by Lisle (1994). Roberts (2001) presented a systematic classification of seismic curvature attributes and the implementation of 2D surface curvature that was applied to predict fracture orientation and distribution. Hart (2002) showed that strike curvature is highly correlated with open fractures in northwestern New Mexico. The first generation of curvature attribute was 2D surface curvature calculated using horizon data, which did not directly use the seismic amplitude. The deviation and the distortion caused by the misclosure in horizon tracking will have a seriously impact on the surface curvature and can thus easily lead to structural artifacts (Al-Dossary and Marfurt, 2006; Blumentritt et al., 2006; Chopra and Marfurt, 2007a; 2007b; 2008). To overcome the limitations of 2D surface curvature, a second generation of curvature attributes was proposed, i.e., volumetric curvature (Al-Dossary and Marfurt, 2006; Blumentritt et al., 2006; Klein et al., 2008), which directly utilize the seismic amplitude.

In summary, coherence measure lateral discontinuity in seismic waveforms, whereas curvature is a measurement of structural deformation. They are mathematically independent (Chopra, 2009; Mai, 2009)and can be used to identify channels, faults, fracture zones, fold, warps, collapses, flexures, buildups and other geological anomalies. However, the following problems can be encountered in seismic interpretation: First, the characteristic response and sensitivity of the two attributes to the above geological anomalies are similar, but also significantly distinct. A clear understanding of the correlated relationships between these two attributes and geological anomalies requires further comparative analysis by using forward models that include the geological anomalies mentioned above. This analysis can provide definite guidance for actual seismic interpretation. We also need to understand how to utilize the fusion of these two measurements to improve the credibility and distinction of

geological anomalies in characterizing complex reservoirs and in structural interpretation. Chopra and Marfurt (2009; 2010a) applied a scheme to co-render curvature and coherence. They showed curvature images overlain by the corresponding coherence images rendered with a opacity that was indiscriminately set to a certain percentage. The co-rendering implements, to some extent, the fusion of both the curvature and coherence. However, because the interpreters are primarily concerned with low-coherent discontinuity anomalies (i.e. low or no coherent), rendering the whole coherence image with the opacity set to a same percentage will lead to smearing and blurring the geological features of interest.

With reference to the problems mentioned above, this paper provides an approach for computing 3D volumetric curvature based on the complex trace analysis. We then make a comparative analysis of the similarities and differences between the 3D volumetric curvature set and eigenstructure-based coherence by using forward synthetic records from modified "French" models (the French model is explained later). This work thus yields a better understanding of 3D volumetric curvature and coherence as well as their spatial relationships to geological anomalies of interest. Next, we present a combined mapping of co-rendered coherence with most positive curvature and most negative curvature by discriminately choosing and setting the transparency of both eigenstructure-based coherence and 3D volumetric curvature. This "fusion mapping" scheme fully utilizes the effective information and preserves and highlights the geological anomalies as much as possible. The methods are then applied to detect faults and fracture zones within a 3D marine seismic data from ZH field in the Pearl River Mouth Basin in the northern South China Sea, China.

THEORY OF 3D VOLUMETRIC CURVATURE ANALYSIS

In geometric seismology, any reflection point r(t,x,y) on the seismic reflector of a geologic body in three-dimensional space can be considered the time scalar u(t,x,y), and then the gradient grad(u) is the variance ratio along the reflecting surface in different directions, i.e., the first derivative of a curve intercepted on normal section along the direction vector of reflecting surface. The result is the apparent dip vector of this reflection point:

$$\text{grad}(u) = (\partial u/\partial x)\mathbf{i} + (\partial u/\partial y)\mathbf{j} + (\partial u/\partial t)\mathbf{k} = p_x\mathbf{i} + q_y\mathbf{j} + r_t\mathbf{k} \quad , \qquad (1)$$

where p_x, q_y and r_t denote apparent dip components along x, y and t axes, respectively, shown in Fig. 1. θ is true dip, and ϕ is dip azimuth.

Substituting the apparent dip p_x and q_y into eq. (1), we then obtain curvature components in the direction of the x- and y-axes:

$$\begin{cases} C_x = (\partial^2 u/\partial x^2)/[1 + (\partial u/\partial x)^2]^{3/2} = (\partial p_x/\partial x)/(1 + p_x^2)^{3/2} \\ C_y = (\partial^2 u/\partial y^2)/[1 + (\partial u/\partial y)^2]^{3/2} = (\partial q_y/\partial y)/(1 + q_y^2)^{3/2} \end{cases} . \quad (2)$$

The above equation shows that the curvature at any point in 3D space can be calculated by using the dip. Consequently, a 3D curvature cube can be formed.

The apparent dip can be calculated by dip scan or gradient structure tensor (Marfurt et al., 1998). It is also obtained by calculating instantaneous frequency from complex trace analysis (Marfurt, 2006; Luo et al., 1996; Barnes, 1996). Instantaneous parameters can be calculated as follows:

$$\begin{cases} k_x(t,x,y) = \partial\Phi_x/\partial x = [u(\partial u_x^H/\partial x) - u_x^H(\partial u/\partial x)]/[(u)^2 + (u_x^H)^2] \\ k_y(t,x,y) = \partial\Phi_y/\partial y = [u(\partial u_y^H/\partial y) - u_y^H(\partial u/\partial y)]/[(u)^2 + (u_y^H)^2] \\ \omega(t,x,y) = \partial\varphi/\partial t = [u(\partial u_t^H/\partial t) - u_t^H(\partial u/\partial t)]/[(u)^2 + (u_t^H)^2] \end{cases} , \quad (3)$$

where Φ_x and Φ_y denote the space-variant phase in the direction of the x- and y-axes, respectively; φ denotes instantaneous phase. k_x and k_y denote space-variant wave-numbers along the x- and y-axes, respectively, ω denotes instantaneous frequency. u denotes the input seismic data, and u^H denotes its Hilbert transform.

In eq. (3), calculating the three parameters includes more differential operations, so that the computation suffers from lower accuracy and higher sensitivity to noise. To overcome this limitation, we investigate the difference algorithm of instantaneous frequency described by Claerbout (1976). We then use a new central difference scheme to calculate the three parameters with respect to x, y and t below:

$$\begin{cases} k_x(t,x,y) = \partial\Phi_x/\partial x = (1/2\Delta x)\{[u_x^H(x+\Delta x) - u_x^H(x-\Delta x)]u(x) \\ \qquad -[u(x+\Delta x) - u(x-\Delta x)]u_x^H(x)\}/\{u^2(x) + [u_x^H(x)]^2\} \\ k_y(t,x,y) = \partial\Phi_y/\partial y = (1/2\Delta y)\{[u_y^H(y+\Delta y) - u_y^H(y-\Delta y)]u(y) \\ \qquad -[u(y+\Delta y) - u(y-\Delta y)]u_y^H(y)\}/\{u^2(y) + [u_y^H(x)]^2\} \\ \omega(t,x,y) = \partial\varphi/\partial t = (1/2\Delta t)\{[u_t^H(t+\Delta t) - u_t^H(t-\Delta t)]u(t) \\ \qquad -[u(t+\Delta t) - u(t-\Delta t)]u_t^H(t)\}/\{u^2(t) + [u_t^H(x)]^2\} \end{cases} , \quad (4)$$

where the definition of variables in the equation are the same as eq. (3).

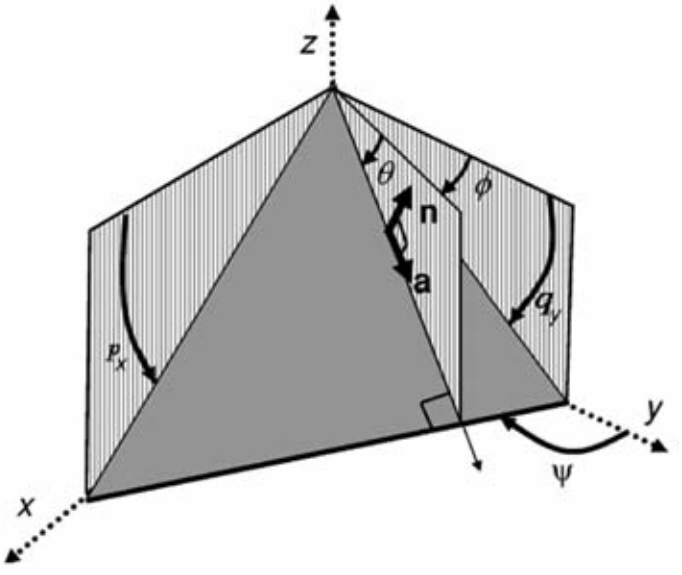

Fig. 1. Seismic reflector dip, azimuth, apparent dip and their relationship (modified from Marfurt, 2006).

After obtaining k_x, k_y and ω by using eq. (3), we then calculate the apparent dip (p_x,q_y):

$$\begin{cases} p_x = k_x/\omega \\ q_y = k_y/\omega \end{cases}, \tag{5}$$

where p_x and q_y denote the apparent dip with respect to x- and y-axes, respectively.

From eq. (2), the curvature at a particular point in 3D space is calculated by a space surface equation fitted from the apparent dip of this point and its neighboring sample points. Then the general expression of N-order surface fitting equation is obtained based on a least squares approximation:

$$z(x,y) = \sum_{i=N}^{0} \left(\sum_{i=j}^{0} c_{i,j-i} x^i y^{j-i} \right) . \tag{6}$$

When N = 2, the quadratic surface equation is obtained:

$$z(x,y) = ax^2 + by^2 + cxy + dx + ey + f . \tag{7}$$

By calculating the differential of the above equation and substituting the

apparent dip p_x and q_y into it, we then obtain:

$$\begin{cases} (\partial/\partial x)(\partial z/\partial x) = \partial p_x/\partial x = 2a \\ (\partial/\partial y)(\partial z/\partial y) = \partial q_y/\partial y = 2b \\ (\partial/\partial y)(\partial z/\partial x) + (\partial/\partial x)(\partial z/\partial y) = (\partial p_x/\partial y) + (\partial q_y/\partial x) = 2c \\ \partial z/\partial x = d \\ \partial z/\partial y = ed \end{cases} . \quad (8)$$

Thus, the coefficients in eq. (7) are:

$$a = \tfrac{1}{2}(\partial p_x/\partial x),\ b = \tfrac{1}{2}(\partial q_y/\partial y),\ c = \tfrac{1}{2}[(\partial p_x/\partial y) + (\partial q_y/\partial x),$$

$$d = p_x,\ e = q_y. \quad (9)$$

The coefficients in eq. (9) can then be used to calculate the curvature attribute set. The most useful subset of curvatures is the normal curvatures that are orthogonal to the projection plane of the surface (Roberts, 2001). The 3D volumetric curvature attribute set can be defined similarly to the surface curvature set presented by Roberts (2001), such as the mean curvature K_{mean}, the Gaussian curvature K_{gauss}, the maximum curvature K_{max}, the minimum curvature K_{min}, the most positive curvature K_{pos}, the most negative curvature K_{neg}, the dip curvature K_{dip}, the strike curvature K_{strike} and the shape index K_{shape}. They are calculated by the formula below:

$$K_{mean} = [a(1+e^2) + b(1+d^2) - cde]/(1 + d^2 + e^2)^{1/2} \quad (10a)$$

$$K_{gauss} = (4ab - c^2)/(1 + d^2 + e^2)^{1/2} \quad (10b)$$

$$K_{max} = K_{mean} + (K_{mean}^2 - K_{gauss})^{1/2} \quad (10c)$$

$$K_{min} = K_{mean} - (K_{mean}^2 - K_{gauss})^{1/2} \quad (10d)$$

$$K_{pos} = (a + b) + [(a - b)^2 + c^2]^{1/2} \quad (10e)$$

$$K_{neg} = (a + b) - [(a - b)^2 + c^2]^{1/2} \quad (10f)$$

$$K_{dip} = 2(ad^2 + be^2 + cde)/[(d^2 + e^2)(1 + d^2 + e^2)^{3/2}] \quad (10g)$$

$$K_{strike} = 2(ad^2 + be^2 - cde)/[(d^2 + e^2)(1 + d^2 + e^2)^{1/2}] \quad (10h)$$

$$K_{shape} = (2/\pi)\tan^{-}[(K_{min} + K_{max})/(K_{min} - K_{max}) . \quad (10i)$$

In the above curvature attributes, the most positive curvatures K_{pos} and the most negative curvatures K_{neg} are the most useful in delineating faults, fractures, flexures, and folds (Al-Dossary and Marfurt, 2006; Chopra, 2007a; Chopra, 2007b). These two measurements are easy to link directly to geological structure (Chopra,2008). The delineation of several typical geological structures from the combination of K_{pos} and K_{neg} is summarized in Fig. 2, and the macroscopic structural shapes can be defined only using these two measurements.

The fault delineation from K_{pos} and K_{neg} is shown in Fig. 3, with K_{pos} extreme at the endpoint of the downthrown side and K_{neg} extreme at the endpoint of the upthrown side (respectively corresponding to the concave downward and upward). Note that the zero curvature represents the fault displacement (or the inclined fault plane).

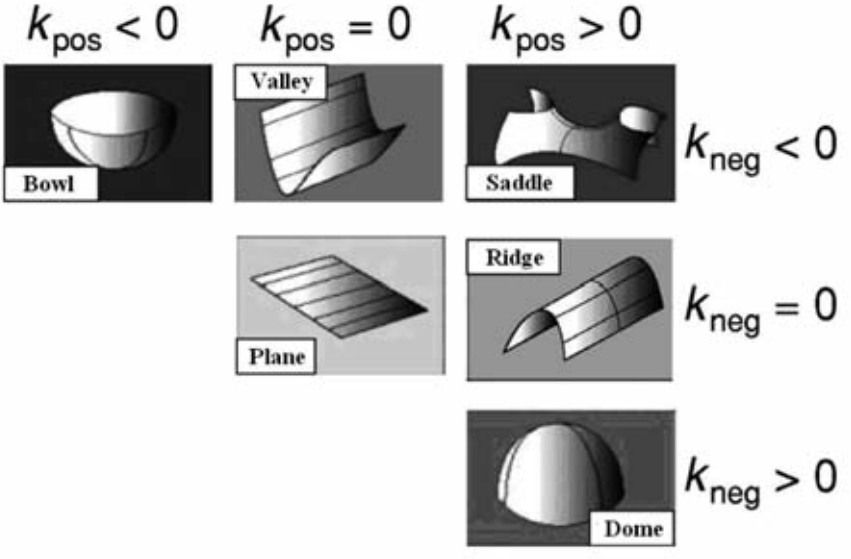

Fig. 2. Relationships between structural shapes and most positive curvature K_{pos}, most negative curvature K_{neg} (Al-Dossary and Marfurt, 2006).

THE COMPARATIVE ANALYSIS OF MODEL-BASED SIMULATION

To visually illustrate the main features of the 3D volumetric curvature and coherence attributes corresponding to different geological structures, we use modifications of the French model (French, 1974), with some geological features added. The following is the background of the French model:

In the mid 1970's, the University of Houston produced a classic model by the physical acquisition of marine seismic data in a water tank over a 3D object.

Known as "the French model" (after designer William S. French), this model proved to be a key vehicle to illustrate the fundamental differences in 2D and 3D migration of seismic data. Used for years by geophysicists as a benchmark to measure the quality of their migration algorithms, the French model significantly advanced the cause of 3D seismic acquisition in exploration and development, and it nicely illustrated imaging theory to geologists and geophysicists alike. Due to its lack of field acquisition costs and its ability to provides results with no interpretation ambiguity, the model has significantly advanced both the art and the application of geophysics in the oil and gas industry.

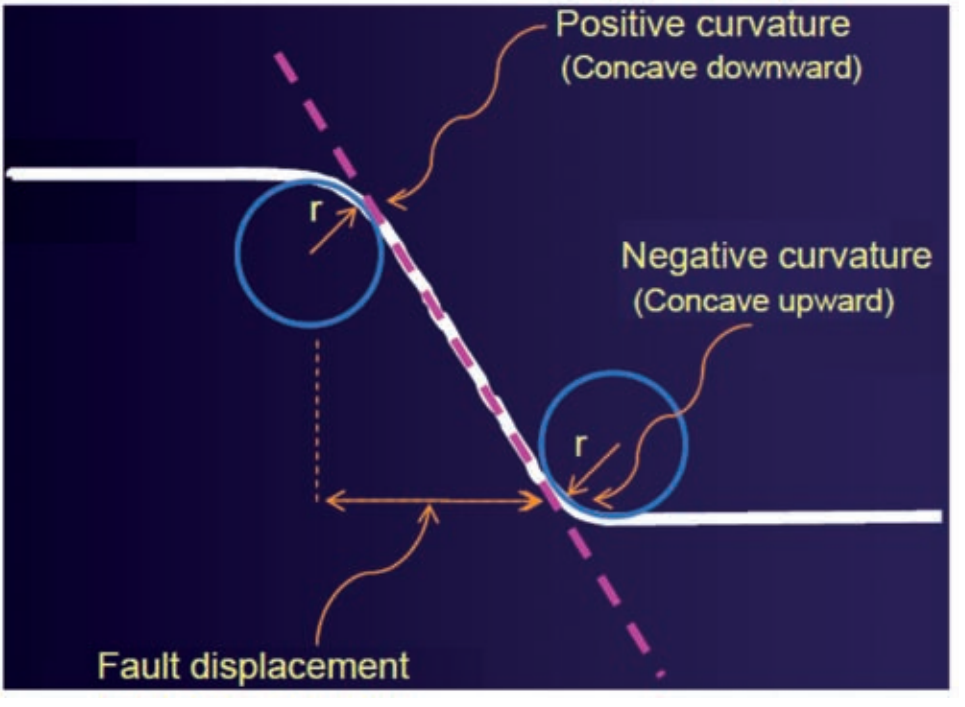

Fig. 3. Fault delineation based on most positive curvature and most negative curvature (modified from Chopra and Marfurt, 2010b).

3D VOLUMETRIC CURVATURE AND COHERENCE OF THE MODELS

To the first modified French model, we added a meandering channel (Fig. 4a). We use this model to simulate the geological features such as a dome, plane, fault (including the dipping fault plane), and meandering channel (Fig. 4). We tracked the target horizon of interest; its time structure map is shown in Fig 4b, and the 3D volumetric curvatures and coherence shown below (Fig. 5) are all extracted from along this horizon.

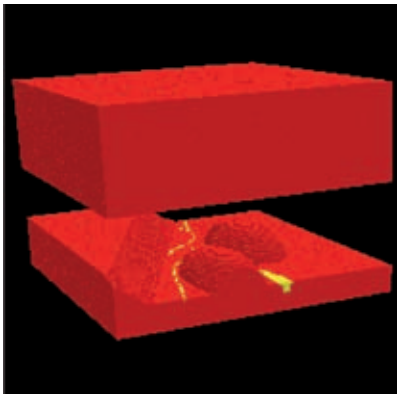

(a)

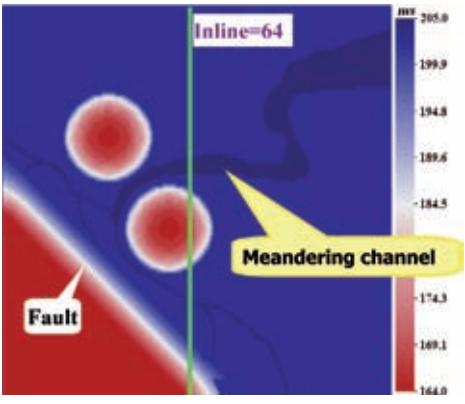

(b)

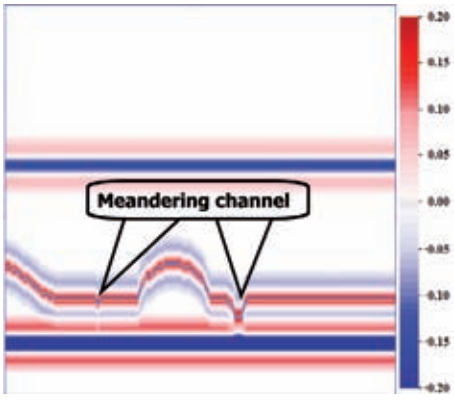

(c)

Fig. 4. Modified French model with a meandering channel added. (a) 3D view of the model; (b) time structure map of the target horizon; (c) synthetic seismic vertical section at Inline=64, note that the horizon is mapped by a blue line.

The curvatures based on the above algorithms and coherence of the model in Fig. 4 are calculated (Fig. 5). Note the coherence slice in Fig. 5a, with a range of 0-1, where 0 (black) denotes no coherence, and 1 (white) represents full coherence. The dome, meandering channel, and fault in Fig. 5a all show low values of coherence (indicating the poor lateral continuity); the plane shows higher values of coherence (i.e., better lateral continuity).

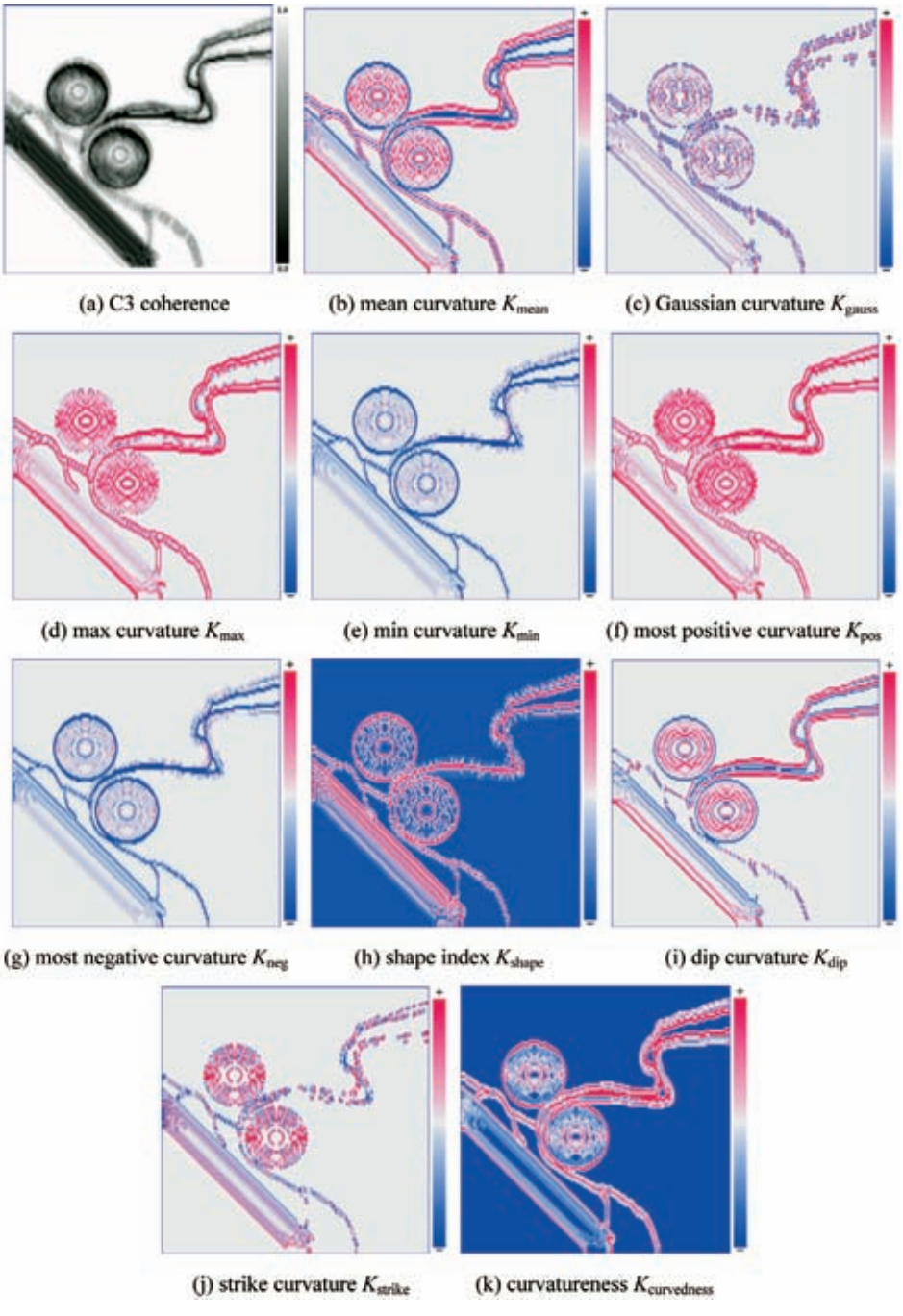

Fig. 5. 3D volumetric curvature set and coherence slices of the model in Fig.4. (a) C3 coherence; (b) mean curvature K_{mean}; (c) Gaussian curvature K_{gauss}; (d) max curvature K_{max}; (e) min curvature K_{min}; (f) most positive curvature K_{pos}; (g) most negative curvature K_{neg}; (h) shape index K_{shape}; (i) dip curvature K_{dip}; (j) strike curvature K_{strike}; (k) curvatureness $K_{curvedness}$.

Comparing Fig. 5d with Fig. 5f, and Fig. 5e with Fig. 5g, respectively, we find $K_{max} \approx K_{pos}$ and $K_{min} \approx K_{neg}$, which are the same observations mentioned by Al-Dossary and Marfurt (2006). On the most positive curvature slice (Fig. 5f), high positive values are seen at the concave downward dome, the endpoint of downthrown side of the fault, and the edge of the meandering channel. The most negative curvature slice (Fig. 5g) shows low negative value at the spatial edge of the dome (i.e., concave upward feature), the endpoints of the upthrown side of the fault, and the position close to the channel bed. Thus, the delineation of same geological properties on K_{pos} and K_{neg} are different, and they also have different spatial relationships with the underlying geologic features.

However, the fault mapped on the coherence slice (in Fig. 5a) indicates only the spatial distribution of fault displacement (i.e., the spatial distribution of inclined fault plane). The coherence is inadequate to directly identify which are the upthrown and downthrown side of faults, the exact spatial location and their contact relationships. The inclined fault plane shows very low values (close to zero) on the K_{pos} and K_{neg} slices. Thus, this could easily be misinterpreted as a horizontal structure that has better lateral continuity on coherence. This potential ambiguity can be considered a deficiency in the curvature attribute relative to the coherence attribute.

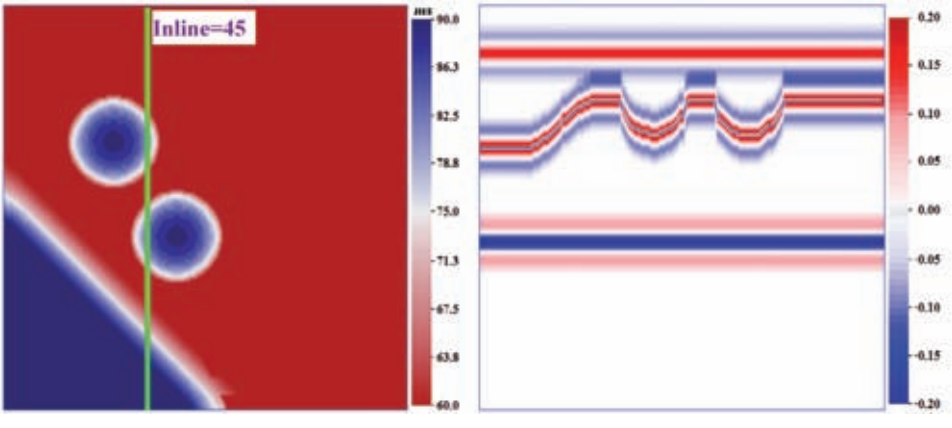

Fig. 6. An inverted French model. (a) time structure map of the target horizon; (b) synthetic seismic vertical section at Inline = 45; note that the horizon is indicated by a blue line.

The second modified French model, shown in Fig. 6, was obtained by inverting the original French model to simulate the geological features such as bowl and fault (note the spatial location of upthrown and downthrown sides and their contact relationships differs from the model in Fig. 4). The time structure map of the tracked target horizon is shown in Fig 6a. The 3D volumetric curvatures and coherence shown below (Fig. 7) are all extracted along this horizon.

The 3D volumetric curvature set and coherence slices for the model in Fig. 6 are shown in Fig. 7. We now compare the coherence slice in Fig. 5a with Fig. 7a. We know that a dome was used in the model used in Fig. 5a, whereas a bowl was used in the model used for Fig. 7a. In addition, the fault dip, spatial position of upthrown and downthrown side in the two models are all different. However, the coherence response from these different geological features is almost identical in Fig. 5a and Fig. 7a. This illustrates that the different geological features such as these are difficult to discriminate exclusively using coherence.

On the most positive curvature slice (Fig. 7f), high positive values illuminate the spatial edge of bowl (i.e., concave downward feature) and the endpoint of the downthrown side of the fault. The most negative curvature slice (Fig. 7g) illustrates low negative value at the endpoint of upthrown side of the fault and the whole bowl (i.e., concave upward feature). In addition, comparing the K_{pos} in Fig. 5f with that in Fig. 7f, and the K_{neg} in Fig. 5g with that in Fig. 7g, respectively, the features such as bowl and dome, the different fault dip, and the spatial variation of upthrown and downthrown sides of the faults are all easily differentiated on the K_{pos} and K_{neg} slice. However, these different geological features and spatial contact relationships are difficult to discriminate on the coherence slice - (c.f. Fig. 5a and Fig. 7a).

THE CO-RENDERING OF 3D VOLUMETRIC CURVATURE AND COHERENCE

From the above comparative analysis of model-based 3D volumetric curvature sets and coherence, we have insight into their respective advantages and disadvantages. It is clear that coherence is superior for delineating the spatial distribution of fault displacement (e.g., fault plane). However, it is difficult to differentiate and identify the fault types, or the spatial contact relationships between upthrown and downthrown sides of a fault using only coherence. In addition, coherence is unable to precisely delineate the different types of stratal bending caused by various structural deformations, such as dome, bowl and fold. However, 3D volumetric curvature K_{pos} and K_{neg} can distinguish precisely between dome and bowl, and identify folds, fault types, and the spatial relationships of the upthrown and downthrown sides of a fault.

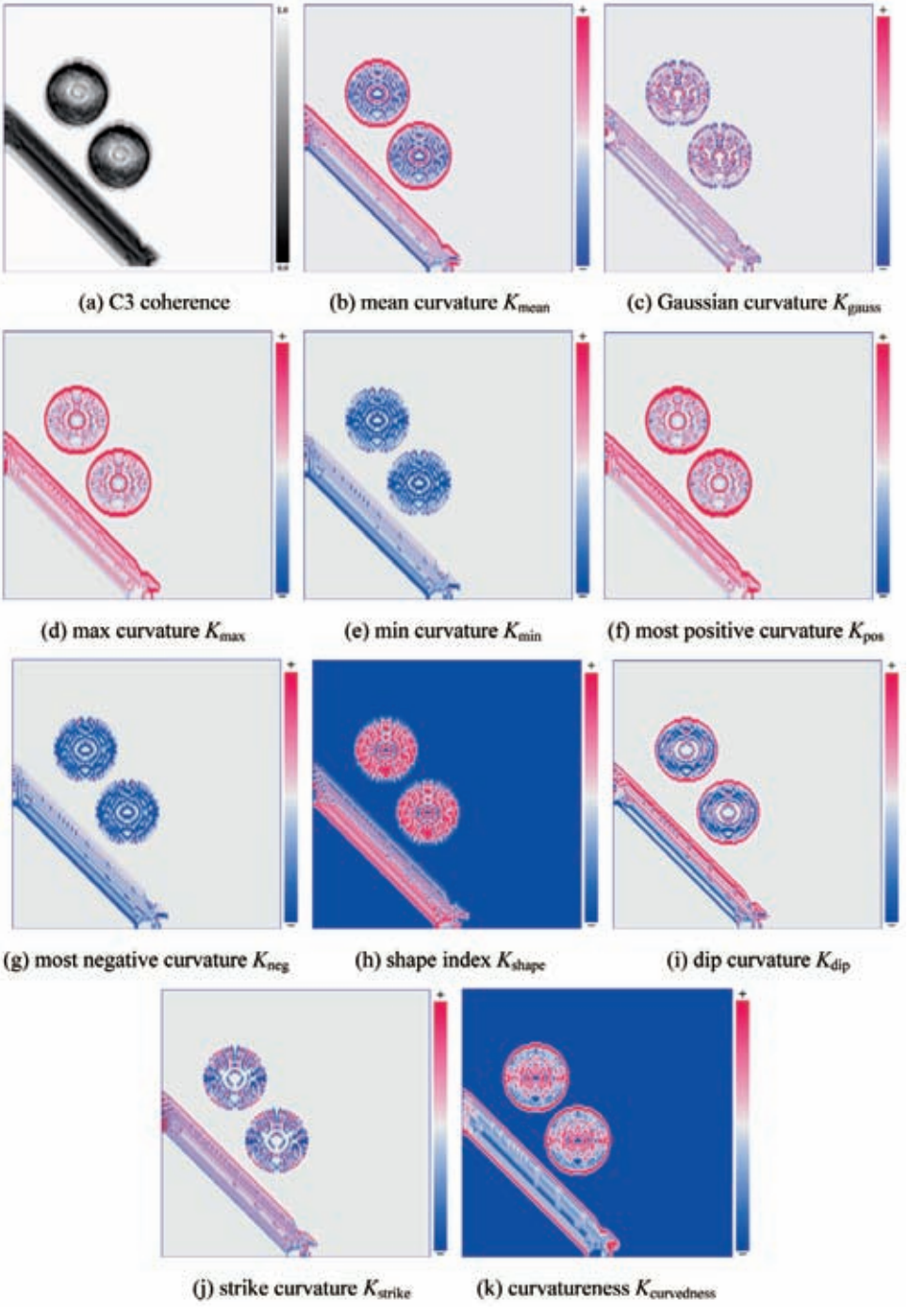

Fig. 7 3D volumetric curvature set and coherence of the model in Fig.6; (a) C3 coherence; (b) mean curvature K_{mean}; (c) Gaussian curvature K_{gauss}; (d) max curvature K_{max}; (e) min curvature K_{min}; (f) most positive curvature K_{pos}; (g) most negative curvature K_{neg}; (h) shape index K_{shape}; (i) dip curvature K_{dip}; (j) strike curvature K_{strike}; (k) curvatureness $K_{curvedness}$.

For some geologic features such as dipping planes (e.g., fault plane) with lateral discontinuity and planes with better lateral continuity, curvature attributes have difficulty in discrimination because of their similar responses. Therefore, some geologic features of interest, such as fault planes, may be easily missed if using this attribute.

In the interpretation of real seismic data, the problems mentioned above will become more complicated and prominent due to the complex diversity of reservoir structure and tectonic features. Therefore, in order to fully extract and highlight geological anomalies, reduce ambiguity, and enhance the reliability of characterizing the reservoir and in structural interpretation, it is useful to co-render coherence with curvatures and merge together the effective information they each measure.

We therefore propose a visual fusion to co-render 3D volumetric curvature with coherence. Coherence is a measurement of lateral discontinuity in seismic waveforms, whereas curvature measures the stratal bending caused by structural deformation. Seismic interpreters are generally most concerned with seismic singularities such as low-coherence discontinuity anomalies (i.e., low or no coherence) and the strata-bending-associated higher-curvature anomalies. Thus, we discriminately choose and set the transparency of eigenstructure-based coherence and 3D volumetric curvature (i.e., lower-coherence discontinuities are set to opaque, whereas higher-coherence values are set to mostly or fully transparent). At the same time, higher value curvatures are set to more opaque. Then we co-render the K_{pos} and K_{neg} images overlain by the corresponding eigenstructure-based coherence map. Such a workflow preserves the discontinuity features of the coherency slice and adds structural bending information measured by curvature at the same time.

Taking the first model in Fig. 4, for example, we test four different types of co-rendering schemes using the K_{pos}, K_{neg} and eigenstructure-based coherence. The first co-rendering image, shown in Fig. 8a, sets the values close to positive maxima (in red) of K_{pos} and the values close to negative minima (in blue) of K_{neg} to opacity, with other values set to high transparency. The endpoints of the upthrown and downthrown side of the normal fault, the dome and its edge, both the edge and the features close to the channel bed, and their spatial distribution are all simultaneously imaged, but the dipping fault plane image appears as a simple plane. Fig. 8b is the second type of co-rendering image, created by setting the values close to positive maxima (in red) of K_{pos} and the values close to zero (in black) of coherence to opacity, with other values set to full transparency. This scheme simultaneously delineates the endpoint of the upthrown side (in red) and the fault plane distribution. The third co-rendering image, shown in Fig. 8c, is created by setting the values close to negative minima (in blue) of K_{neg} and the values close to zero (in black) of coherence to opacity, with other values set to full transparency. Corresponding to Fig. 8b,

Fig. 8c simultaneously illustrates the endpoint of the downthrown side (in blue) and the fault plane distribution. The fourth co-rendering image in Fig. 8d merges the scheme from Figs. 8a-c, by setting the values close to positive maxima (in red) of K_{pos}, the values close to negative minima (in blue) of K_{neg}, and the values close to zero (in black) of coherence to opacity, with other values set to full transparency. The direct delineation of normal fault type, the endpoint

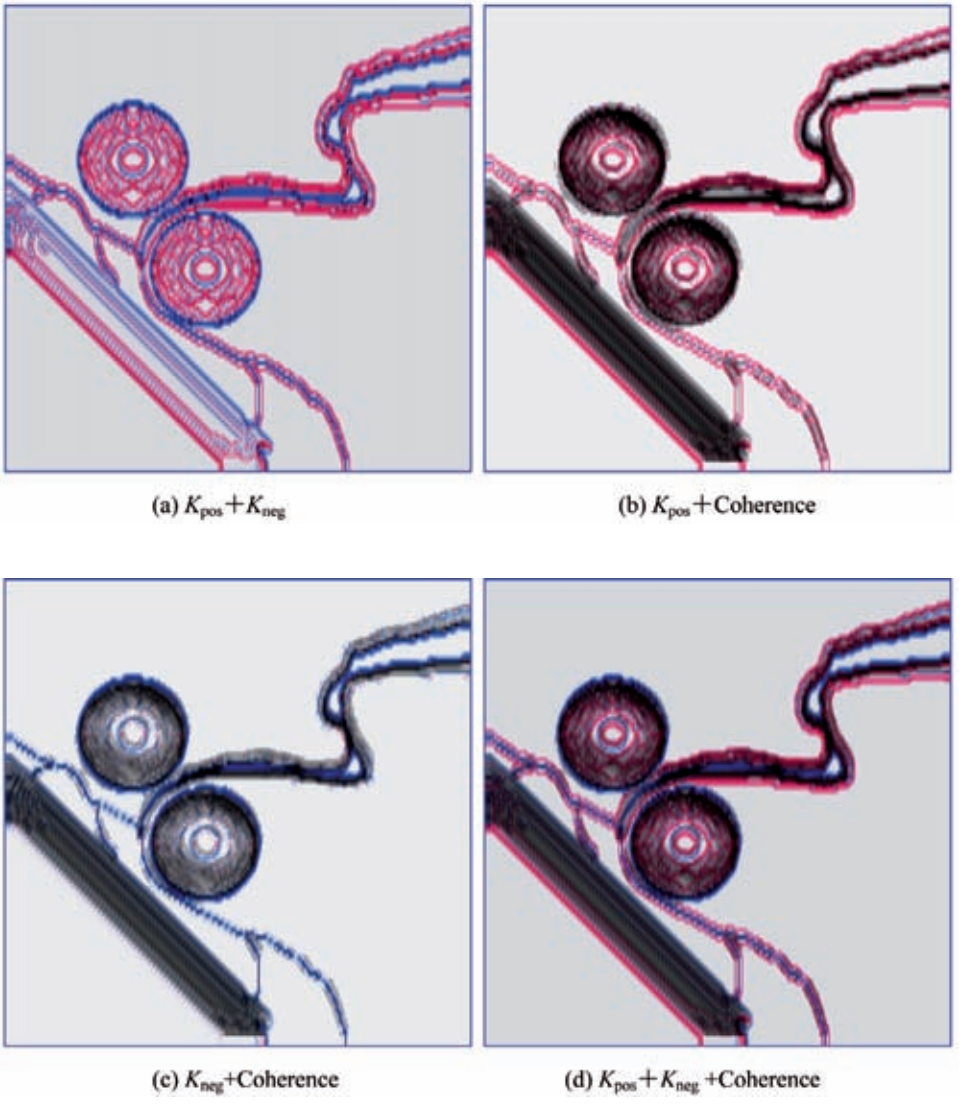

Fig. 8. Four co-rendering maps of K_{pos}, K_{neg} and coherence; (a) K_{pos} + K_{neg}; (b) K_{pos} + Coherence; (c) K_{neg} + Coherence; (d) K_{pos} + K_{neg} + Coherence.

position of the upthrown and downthrown side, the fault plane, dome and its edge, the channel distribution and its internal discontinuity (such as the edge, and the slope variation of the channel bed), and the spatial relationships of these geologic features are all now shown in one map. This demonstrates that the co-rendering schemes allow us to fully reveal the complex reservoir structure and tectonic features and reduce the uncertainty in seismic interpretation.

FIELD DATA EXAMPLE

The methodology described in this paper is now applied to a 3D marine seismic data volume from the ZH field, located in the Pearl River Mouth Basin in the northern South China Sea, China. Acquisition footprints exist in the data set. Neogene limestone is present across the entire 3D survey at the target horizon on which we are focused.

Fig. 9 contains slices extracted along the top of the target limestone horizon on which a wide range of faults and fractures is distributed. On the 3D volumetric curvature K_{pos} and K_{neg} slices (Figs. 9c-d), the various faults, fracture zones and their detail can be clearly identified, and there are fine en-echelon faults on the southeast (indicated by red arrows). However, on the conventional surface curvature slices (Figs. 9a-b), the fine faults and fractures are to some extent smeared or ignored (indicated by cyan arrows), and the background noise is more apparent (indicated by the black rectangle). In comparison with the eigenstructure-based coherence in Fig. 9e, the 3D volumetric curvature, especially K_{neg} (Fig. 9d), provides a superior delineation of faults, fracture zones (indicated by cyan arrows), and en-echelon faults (indicated by red arrows). However, the coherence slice shows a somewhat weaker acquisition footprint than the curvature slices. This demonstrates that curvature attribute is relatively more sensitive to noise.

We show five co-rendering slices in Fig. 10. The first four slices (Figs. 10a-d) are co-rendered using our proposed methodology. The fifth slice (Fig. 10e) is co-rendered in a manner similar to the scheme presented by Chopra and Marfurt (2009; 2010a), in which curvature images are overlain by coherence images rendered with the opacity that set to 75%. The delineation of geological features on each slice (Figs. 10a-d) is superior to the single attribute slices in Fig. 9c-e. In comparison with the co-rendering slice in Fig. 10e, Fig. 10d shows the faults and fractures more clearly and prominently. Furthermore, Fig. 10d shows a less noisy background (e.g., weaker acquisition footprint) than Fig.10e.

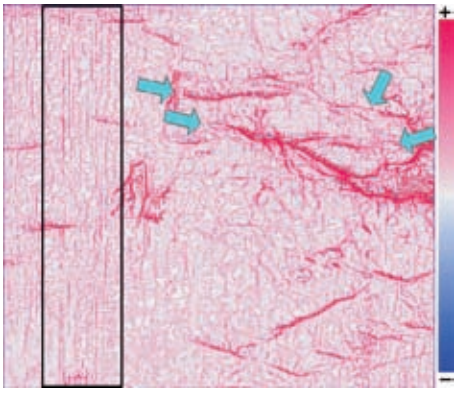

(a)

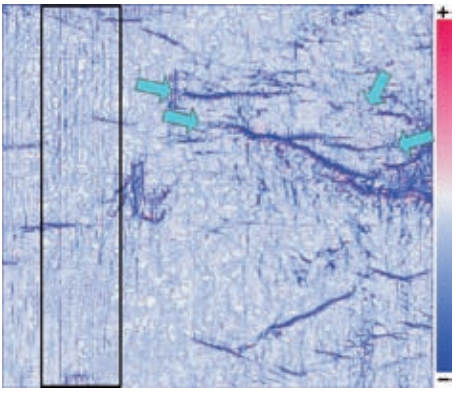

(b)

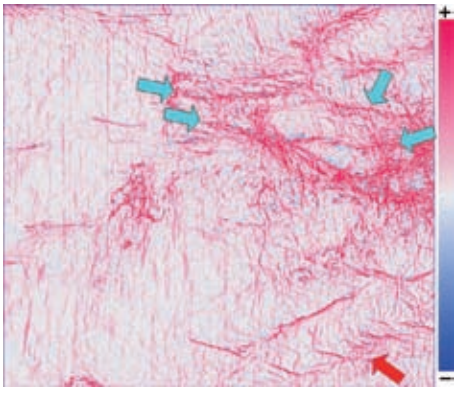

(c)

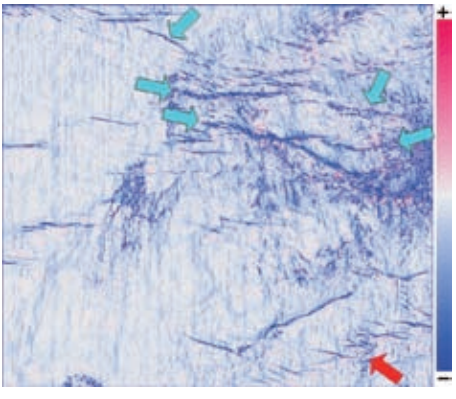

(d)

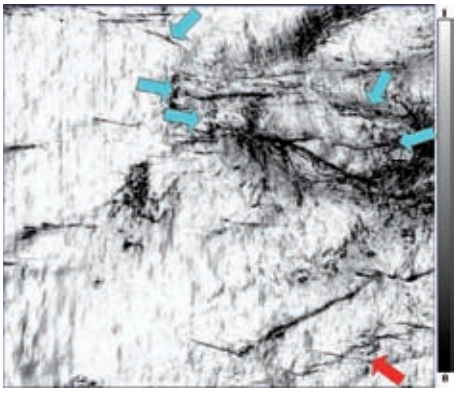

(e)

Fig. 9. The conventional surface curvatures (a) K_{pos} ,(b) K_{neg}; The 3D volumetric curvatures (c) K_{pos}, (d) K_{neg}. (e) C3 coherence.

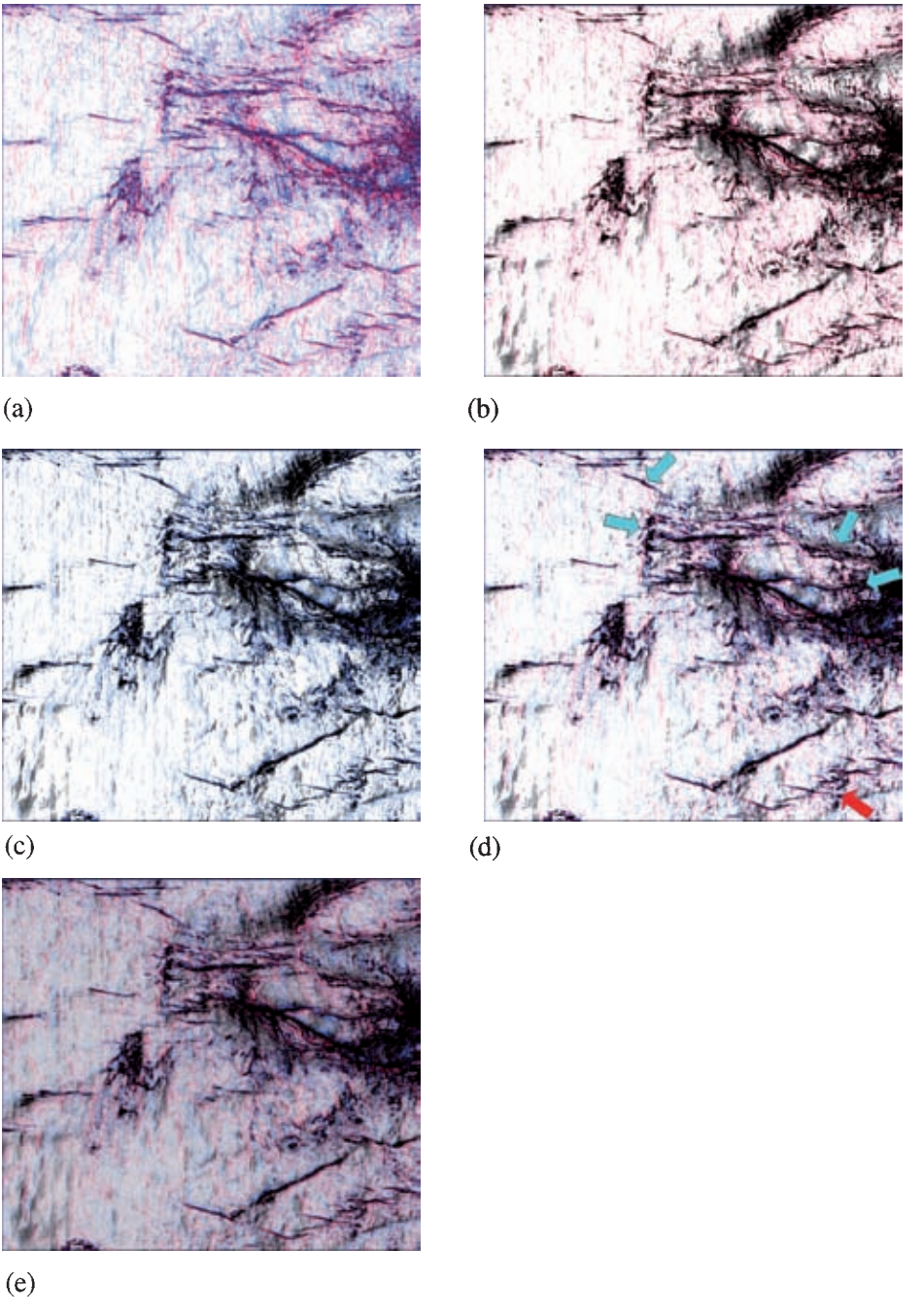

Fig. 10. Five co-rendering slices of K_{pos}, K_{neg} and eigenstructure-based coherence; (a) K_{pos} + K_{neg}, (b) K_{pos} + Coherence, (c) K_{neg} + Coherence and (d) K_{pos} + K_{neg} + Coherence are co-rendered by the methodology discussed in this paper; (e) K_{pos}, K_{neg} and co-rendered with coherence (opacity = 75%). Note that the co-rendering of (e) follows the scheme of Chopra and Marfurt (2009; 2010a).

CONCLUSIONS

The implementation of 3D volumetric curvature in this paper is derived directly from complex trace analysis. The algorithms have the advantages of being easy to implement and having higher computational efficiency. As two of the more superior seismic geometric attributes, 3D volumetric curvature and coherence have both similarities and differences in delineation of faults, fracture zones, lineaments, lithologic distribution of reservoirs, and their lateral variations. The co-rendering scheme presented in the paper provides a powerful tool to fully utilize the geological anomalies indicated by these two attributes, and the method can precisely locate the spatial distribution and the edges of such geologic anomalies. This methodology can reduce ambiguity and uncertainty, improve efficiency and enhance the reliability of interpretations of geological features, reservoir architecture, and structure.

ACKNOWLEDGEMENTS

This work was supported by the National Natural Science Foundation of China (Grant No. 41004054) and the Cultivating Program of Middle-aged Backbone Teachers of Chengdu University of Technology. We greatly thank the anonymous reviewer for the constructive comments and editorial suggestions that significantly improved the quality of the manuscript. The authors acknowledge their colleague Mr. Yongguo Wu at BGP Inc., China National Petroleum Corp., for his help with the synthetic models. This research was also supported by the Cultivating Programme of Excellent Innovation Team of Chengdu University of Technology (Grant No. KYTD201002).

REFERENCES

Al-Dossary, S. and Marfurt, K.J., 2006. 3D volumetric multispectral estimates of reflector curvature and rotation. Geophysics, 71: P41-P51.

Bahorich, M. and Farmer, S.L., 1995. 3-D seismic discontinuity for faults and stratigraphic features: the coherence cube. The Leading Edge, 14: 1053-1058.

Barnes, A.E., 1996. Theory of 2-D complex seismic trace analysis. Geophysics, 61: 264-272.

Blumentritt, C.H., Marfurt, K.J. and Sullivan, E.C., 2006. Volume-based curvature computations illuminate fracture orientations-Early to mid-Paleozoic, Central Basin Platform, West Texas. Geophysics, 71: P41-P51.

Buck, D.M., Alam, A. and Taylor, J.D., 2007. Fractured reservoir prediction from 3D seismic volumetric curvature and low frequency imaging. Expanded Abstr., 77th Ann. Internat. SEG Mtg., San Antonio: 422-426.

Chopra, S. and Marfurt, K.J., 2007. Seismic Attributes for Prospect Identification and Reservoir Characterization. SEG, Tulsa, USA.

Chopra, S. and Marfurt, K.J., 2007. Curvature attribute applications to 3D surface seismic data. The Leading Edge, 26: 404-414.

Chopra, S. and Marfurt, K.J., 2007. Volumetric curvature attributes add value to 3D seismic data interpretation. The Leading Edge, 26: 856-867.

Chopra, S. and Marfurt, K.J., 2008. Emerging and future trends in seismic attributes: The Leading Edge, 27: 298-318.

Chopra, S. and Marfurt, K.J., 2009. Detecting stratigraphic features via crossplotting of seismic discontinuity attributes and their volume visualization. The Leading Edge, 28: 1422-1426.

Chopra, S. and Marfurt, K.J., 2010a. Integration of coherence and volumetric curvature images. The Leading Edge, 29: 1092-1106.

Chopra, S. and Marfurt, K.J., 2010b. Delineating fractures from seismic attributes. Search and Discovery Article #110124.

Claerbout, J.F., 1976. Fundamentals of Geophysical Data Processing. McGraw-Hill Book Company, New York.

Flierman, W., Weide, J.G., Wever, A., Brouwer, F. and Huck, A., 2008. Use of spatial, frequency and curvature attributes for reservoir, fluid and contact predictions. Expanded Abstr., 78th Ann. Internat. SEG Mtg., Las Vegas: 1521-1525.

French, W.S., 1974. Two-dimensional and three-dimensional migration of model-experiment reflection profiles. Geophysics, 39: 265-277.

Gersztenkorn, A. and Marfurt, K.J., 1999. Eigenstructure-based coherence computations as an aid to 3-D structural and stratigraphic mapping. Geophysics, 64: 1468-1479.

Hart, B.S., 2002. Validating seismic attributes: Beyond statistics. The Leading Edge, 21: 1016-1021.

Klein, P., Richard, L. and James, H., 2008. 3D curvature attributes: a new approach for seismic interpretation. First Break, 26: 105-112.

Lisle, R.J., 1994. Detection of zones of abnormal strains in structures using Gaussian curvature analysis. AAPG Bull., 78: 1811-1819.

Luo, Y., Higgs, W.G. and Kowalik, W.S., 1996. Edge detection and stratigraphic analysis using 3D seismic data. Expanded Abstr., 66th Ann. Internat. SEG Mtg., Denver: 324-327.

Mai, H.T., Marfurt, K.J. and Chávez-Pérez, S., 2009. Coherence and volumetric curvatures and their spatial relationship to faults and folds, an example from Chicontepec basin, Mexico. Expanded Abstr., 79th Ann. Internat. SEG Mtg., Houston: 1063-1067.

Marfurt, K.J., Kirlin, R.L., Farmer, S. and Bahorich, M., 1998. 3-D seismic attributes using a semblance-based coherency algorithm. Geophysics, 63: 1150-1165.

Marfurt, K.J., Sudhaker, V., Gersztenkorn, A., Crawford, K.D. and Nissen, S.E., 1999. Coherency calculations in the presence of structural dip. Geophysics, 64: 104-111.

Marfurt, K.J., 2006. Robust estimates of 3D reflector dip and azimuth. Geophysics, 71: P29-P40.

Roberts, A., 2001. Curvature attributes and their application to 3D interpreted horizons. First Break, 19: 85-100.